surfaces

MDPI

Article

Photoelectrochemical and Structural Insights of Electrodeposited CeO_2 Photoanodes

Alberto E. Molina-Lozano [1], Marcos R. V. Lanza [2], Pablo Ortiz [3] and María T. Cortés [1,*]

[1] Department of Chemistry, Universidad de los Andes, Bogotá 111711, Colombia
[2] São Carlos Institute of Chemistry, University of São Paulo, Avenida Trabalhador São Carlense 400, São Carlos 13566-590, Brazil; marcoslanza@usp.br
[3] Department of Chemical Engineering, Universidad de los Andes, Bogotá 111711, Colombia
* Correspondence: marcorte@uniandes.edu.co

Abstract: Cerium dioxide (CeO_2) is a promising material for photoelectrochemical applications, requiring a thorough understanding of the interplay between its properties and structure for optimal performance. This study investigated the photoelectrochemical performance of CeO_2 photoanodes immobilized by electrodeposition on glass substrates, focusing on the correlation between the annealing temperature and structural, optical, and electrical changes. CeO_2 coatings were obtained via chronoamperometry in an aqueous solution of 25 mM $CeCl_3$ and 50 mM $NaNO_3$. The photoelectrochemical characterization included the evaluation of photoactivity, current density, stability, and recombination using linear sweep voltammetry (LSV) and chronoamperometry (CA). Charge transfer resistance, flat-band potential, and capacitance were assessed through impedance spectroscopy. The optimal annealing temperature for this material was found to be 600 °C as it resulted in the lowest charge transfer resistance and increased photocurrent, which was attributed to enhanced crystallinity and variations in the Ce^{3+}/Ce^{4+} ratio.

Keywords: CeO_2; electrochemical properties; photoelectrodes; coating

check for updates

Citation: Molina-Lozano, A.E.; Lanza, M.R.V.; Ortiz, P.; Cortés, M.T. Photoelectrochemical and Structural Insights of Electrodeposited CeO_2 Photoanodes. *Surfaces* **2024**, *7*, 898–919. https://doi.org/10.3390/surfaces7040059

Academic Editor: Gaetano Granozzi

Received: 2 September 2024
Revised: 1 October 2024
Accepted: 9 October 2024
Published: 19 October 2024

Copyright: © 2024 by the authors. Licensee MDPI, Basel, Switzerland. This article is an open access article distributed under the terms and conditions of the Creative Commons Attribution (CC BY) license (https://creativecommons.org/licenses/by/4.0/).

1. Introduction

Cerium dioxide (CeO_2) has remarkable optical and photoelectronic properties, making it an important rare earth oxide. This oxide finds applications in various environmental fields such as solar cells, water splitting, and pollutant degradation. The main advantages of CeO_2 for photocatalysis include its ability to store oxygen by varying the oxidation state (Ce^{3+}/Ce^{4+}), absorb visible light, be chemically stable, and be biocompatible. In addition, it is abundant and inexpensive [1].

CeO_2 for photocatalytic applications is obtained by several methods and one of the most used is hydrothermal synthesis [2,3]. Hydrothermal synthesis presents a compelling methodology for the fabrication of CeO_2 nanoparticles, particularly for photocatalytic applications, due to its ability to produce materials with controlled morphology, crystallinity, and particle sizes [4,5]. Nevertheless, this method requires long reaction times, high-pressure conditions, and the use of hazardous reagents [6]. Therefore, it is advisable to employ alternative synthesis strategies that entail fewer environmental repercussions and reduced synthesis risks.

A much less explored but more versatile and affordable synthesis technique for obtaining CeO_2 is electrodeposition. This method offers important advantages, including the need for low concentrations of Ce^{3+} precursor salts, low electrical signals (potential or current), and short synthesis times [7]. Additionally, electrodeposition facilitates the use of templates to achieve morphological diversity in oxides, thereby enabling control over their surface area. Importantly, for photocatalytic applications, this technique allows the formation of oxides, such as fluorine-doped tin oxide (FTO)-[8] and indium-doped tin oxide (ITO) [9]-coated glassy substrates, directly on transparent electrodes. However,

despite these notable advantages, electrodeposition as a method of photocatalyst synthesis has been little explored.

CeO_2 coatings can be electrodeposited through electrophoretic deposition, wherein charged and suspended CeO_2 nanoparticles migrate towards the electrode surface under the influence of a strong electric field [10]. Alternatively, direct electrodeposition involves the application of a potential or current to the electrode, promoting the formation of a CeO_2 layer [11]. In cathodic electrodeposition, a negative potential is used to induce the formation of OH^- on the electrode surface, which facilitates the migration of cerium cations and the subsequent formation of a hydroxide layer.

A common synthesis medium in cathodic electrodeposition is an aqueous solution containing nitrates, where different electrochemical reactions could occur depending on the applied potential and the pH of the medium (Equations (1)–(4)) [2,12]. These reactions, either by the generation of OH^- or by the consumption of H^+, increase the pH at the solution–electrode interface. As for the Ce^{3+} reduction reaction, it is not thermodynamically favored due to its more negative standard reduction potential (−2.34 V) [13]. Moreover, the electrodeposition of Ce, which is mediated by the basic medium produced at the interface, takes place according to Reactions (5) and (6) [14]:

$$2H_2O + 2e^- \rightarrow H_2 + 2OH^- \quad (1)$$

$$2H_3O^+ + 2e^- \rightarrow H_2 + 2\ H_2O \quad (2)$$

$$O_2 + 2H_2O + 4e^- \rightarrow 4OH^- \quad (3)$$

$$NO_3^- + H_2O + 2e^- \rightarrow NO_2^- + 2OH^- \quad (4)$$

$$Ce^{3+} + 3OH^- \rightarrow Ce(OH)_3 \quad (5)$$

$$4Ce^{3+} + O_2 + 4OH^- + 2H_2O \rightarrow 4Ce(OH)_2^{2+} \quad (6)$$

Finally, the compound is oxidized according to Reactions (7)–(9):

$$Ce(OH)_3 \rightarrow CeO_2 + H_3O^+ + e^- \quad (7)$$

$$Ce(OH)_2^{2+} + 2OH^- \rightarrow CeO_2 + 2H_2O \quad (8)$$

$$Ce(OH)_2^{2+} + 2OH^- \rightarrow Ce(OH)_4 \quad (9)$$

$$4Ce(OH)_3 + O_2 \rightarrow 4CeO_2 + 6H_2O \quad (10)$$

After electrodeposition, the electrode is thermally heated (annealed) to convert the hydroxide to oxide and help remove impurities (Reaction (10)). Importantly, the formation of the $Ce(OH)_3$ coating is controlled not only by the application of a reduction overpotential, which generates hydroxyls and promotes the migration of Ce^{3+} ions to the interface, but also by the easy precipitation of $Ce(OH)_3$ because it requires a low OH^- concentration due to its low solubility product (Ksp = 1.6×10^{-20}) [15].

When the cerium compound is annealed in reactive environment, Ce^{3+} ions can react with oxygen (O^2) molecules in the atmosphere, causing the oxidation of Ce^{3+} to Ce^{4+} [16]:

$$2Ce^{3+} + 1/2O_2 \rightarrow 2Ce^{4+} + O^{2-} \quad (11)$$

In this reaction, the Ce^{3+} ions lose an electron and are oxidized to Ce^{4+}, and while the oxygen molecules are reduced to oxide (O^{-2}), the ions combine to form cerium oxide (CeO_2). The temperature and annealing duration are critical because they determine the rate of oxidation [17]. Higher temperatures and longer annealing times usually favor the conversion of Ce^{3+} to Ce^{4+}, which affects several characteristics that define the optical and electronic properties of the material. These include crystal structure defects, Ce^{3+} and Ce^{4+} concentrations, oxygen vacancies, and CeO_2 surface chemistry [18]. These effects have been studied especially for the oxide obtained in suspension or in the form of nanoparticles.

For example, Sbera et al. recently studied the effect of the heat treatment of chemically prepared CeO_2 powder and determined, by XRD, that annealing significantly improves the crystallinity of the oxide [18]. Also, Acosta-Silva et al. obtained CeO_2 thin films deposited on glass substrates by dip coating and evaluated the effect of annealing [19]. It was observed that increasing the annealing temperature improves the crystallinity of CeO_2, thus increasing the photoactivity and conductivity of the material. In other study, Sumalin Phokha studied the effect of annealing temperature on the structural and magnetic properties of CeO_2 films deposited on silicon substrates by magnetron sputtering [20]. In contrast to the results obtained by Yuliana de Jesus, Phoka et al. found that the annealing of CeO_2 films causes an increase in the lattice defects of the semiconductor, which reduces the crystallinity of the material but improves its magnetic properties.

Although CeO_2 is an extensively studied semiconductor material, it is noteworthy that very little research has been conducted on the performance of electrodeposited CeO_2 films on conductive glass substrates such as FTO or ITO. And there have been no known studies on the effect of annealing on the properties of CeO_2 deposited on these substrates. This is surprising since the use of transparent electrodes is particularly relevant for evaluating the photoactivity and photoelectrochemical performance of semiconductors. These characterizations complement the optical and structural evaluation and give indications of the applicability of the material as a photoelectrode. In some studies, in which CeO_2 was obtained on FTO and on ITO, the optical and chemical properties of the oxide and the influence of some conditions of synthesis were evaluated. This work contributes to the evaluation of the structural, morphological, optical, electrical, and photoelectrochemical properties of CeO_2 layers obtained by electrodeposition on FTO substrates. Specifically, the effect of the annealing temperature (200, 300, 400, 500, and 600 °C) on these properties has been studied here, highlighting that, for the first time, the influence of this temperature on the photoelectrochemical performance of the CeO_2/FTO photoanode has been investigated.

2. Methods

2.1. Materials

Cerium chloride heptahydrate ($CeCl_3 \cdot 7H_2O$, 99.8%), sodium nitrate ($NaNO_3$, 99.5%), sodium sulfate (Na_2SO_4, 98.0%), and sodium hydroxide (NaOH, 99.0%) were purchased from Sigma-Aldrich. Fluorine-doped tin oxide (FTO) glasses were purchased from Ossila. All aqueous solutions were prepared using deionized (DI) water.

2.2. Preparation of FTO Substrates

FTO substrates measuring (2.5 × 0.62) cm were sonicated in a soap solution for 10 min, followed by a 10 min rinse with DI water. Subsequently, they were immersed in a 10% *w*/*v* NaOH solution at 55 °C for 3 min. Finally, the substrates were rinsed twice with DI water for 10 min each time, dried with an air flow, and stored in a petri dish within a desiccator.

2.3. Preparation of CeO_2 Photoanodes

CeO_2 photoanodes were synthesized by electrodeposition using a 0.025 M $CeCl_3 \cdot 7H_2O$ and 0.050 M $NaNO_3$ solution at pH 4.5 (adjusted with 0.1 M NaOH and 0.1 M HNO_3). The FTO substrate served as the working electrode, a Ag/AgCl electrode (saturated in NaCl) was the reference electrode, and a Pt wire was the counter electrode. A cathodic potential of −1.2 V was applied for 300 s to obtain a $Ce(OH)_3$ layer on the FTO glass. Subsequently, the substrates were annealed at various temperatures (200 °C, 300 °C, 400 °C, 500 °C, and 600 °C) for 1 h under an air atmosphere to completely convert the hydroxide to cerium oxide. Finally, the photoanodes were cooled to room temperature in a desiccator.

2.4. Physicochemical Characterization of CeO_2 Photoanodes

The chemical structure of the CeO_2 photoanodes was analyzed using a Raman spectrophotometer (Horiba XploRA™ PLUS, Kawasaki, Japan) equipped with a 532 nm laser (100% intensity) and a range of 300 to 1200 cm^{-1}. The morphology of the CeO_2 layers was

examined using a JEOL scanning electron microscope (model JSM 6490-LV, Tokio, Japan). X-ray diffraction (XRD) experiments were performed using a Rigaku Ultima III diffractometer (Tokio, Japan) with CuKa radiation (1.5406 Å) while the accelerating potential and applied current were maintained at 40 KV and 40 mA, respectively. The UV-Vis spectra were taken using an Analytik Jena SPECORD 50 PLUS spectrometer (Jena, Germany). X-ray photoelectron spectroscopy (XPS) with a Quantera II PHI (Chanhassen, MN, USA) was used to characterize the elemental composition of the CeO_2 −600 °C coating. The Al Kα line (1486.6 eV) operating at 15 kV and 25 W was used as the ionization source.

2.5. Photoelectrochemical Characterization of CeO_2 Photoanodes

All electrochemical experiments, including the synthesis of cerium oxide, were conducted using an Autolab N65 potentiostat–galvanostat (Herisau, Switzerland). Potentials were measured with reference to a Ag/AgCl electrode saturated in NaCl and a Pt wire served as the counter electrode. For the photoelectrochemical characterization of the photoanodes, linear sweep voltammetry (LSV) was performed from 0.5 to 1.2 V vs. AgCl (1.1 to 1.8 vs. RHE) to at a scan rate of 10 mV/s, and chronoamperometry (CA) was conducted at 1.2 V vs. Ag/AgCl (1.8 V vs. RHE) for 300 s. Electrochemical impedance spectroscopy (EIS) measurements were performed applying a perturbation of 10 mV. A range of frequency from 0.1 Hz to 100 KHz at 1.0 V vs. Ag/AgCl (1.6 vs. RHE) was used to perform the impedance measurements. Mott–Schottky (M-S) plots for CeO_2 photoanodes were collected using a frequency of 1000 Hz with a range of potential from −1.2 V to 0.0 V vs. Ag/AgCl. An electrolyte solution of 0.10 M Na_2SO_4 at pH of 7.0 was used. The radiation source was provided by an ABBET solar simulator (100 mW/cm^2).

3. Results and Discussion

3.1. Electrodeposition of CeO_2 Coating on Fto Glass

CeO_2 coatings were synthesized by applying a reducing potential of −1.2 V vs. Ag/AgCl to FTO substrates immersed in an aqueous solution containing 25 mM Ce^{3+} and 50 mM NO_3^- at pH 4.5. Ce^{+3} is stable at this pH and potential according to the Pourbaix diagram for Ce [21]. The application of the reduction potential results in a cathodic current associated with the reduction of nitrate to nitrite with the formation of surface hydroxyl groups (Reaction 4). In addition, the negative polarization favors the migration of Ce^{3+} to the interface where it can react with hydroxyls (Reactions (5)–(6)). Thus, this combination of chemical and electrochemical reactions leads to the electrodeposition of $Ce(OH)_3$ on the FTO substrate when this reduction potential is applied.

The chronoamperogram in Figure S1 shows the current behavior during the electrodeposition process of $Ce(OH)_3$; the observed current peak is associated with the formation of hydroxyls, the nucleation stage, and the overlapping of the growing $Ce(OH)_3$ nuclei according to Reactions (1)–(10). The current decreases due to mass transfer limitations, and finally, the last stage is reached where the current stabilizes and the growth of the $Ce(OH)_3$ layer ends. The current remains at a constant value because the electrode is completely covered with the passivating hydroxide layer. In the study, the cathodic polarization was maintained for 300 s, at the end of which a light brown $Ce(OH)_3$ layer was observed coating the FTO surface (Figure S2A). The final pH of the synthesis solution decreased to 3.1 due to the production of H^+ by the oxygen evolution reaction at the anode of the cell. The current behavior over time agreed with that observed by Yutting Luo for the electrodeposition of CeO_2 on cupper substrates [22].

Following electrodeposition, $Ce(OH)_3$-coated substrates were air-dried and annealed for 1 h to obtain $CeO)_2$. Figure S2B shows the coating obtained on FTO by annealing at 600 °C. The annealing process can have physical and chemical effects on the final properties of the compound: for example, during annealing, water is expelled from the structure, which can influence the lattice parameters of CeO_2. Moreover, in the presence of oxygen, CeO_2 may undergo an exchange of this atom and thus experience a change in the oxidation state of Ce.

According to the literature, the dehydration of cerium hydroxide begins at 200 °C and its decomposition requires higher temperatures: around 400 °C. However, these temperatures may vary depending on environmental conditions and reaction kinetics. To investigate these effects, we conducted a physicochemical characterization of the CeO_2 photoanodes, monitoring their structural, optical, and electrochemical properties across a range of annealing temperatures. The temperature range for this research was constrained by the physicochemical stability of the FTO substrate, which is maintained up to a maximum of 600–700 °C. When CeO_2 is annealed in an oxygen-rich atmosphere, increasing the temperature is expected to affect structural and physical properties that directly influence the photoelectrochemistry of the oxide, such as the crystallinity, microstructure, oxygen vacancies, optical bandgap, and charge transport.

3.2. Effect of Annealing Temperature on the Structural Properties of CeO_2 Photoanodes

3.2.1. XRD

XRD measurements of CeO_2 photoanodes obtained by electrodeposition on FTO and annealed at different temperatures (200, 300, 400, 500, and 600 °C) were performed. Figure 1 shows the X-ray diffraction (XRD) patterns; the diffraction peaks at 28.8°, 33.4°, 47.9°, 56.5°, and 59.2° correspond to the (111), (200), (220), (311), and (222) crystal planes of the cubic fluorite structure of CeO_2 [23]. The diffractograms also show the increase in intensity at all peaks and the decrease in full width at half maximum (FWHM) of peak (111) with an increasing annealing temperature (Table 1). This indicates that the oxide becomes more crystalline with an increasing annealing temperature. It is likely that a higher annealing temperature favors the reaction of CeO_2 with atmospheric oxygen, promoting its oxidation to Ce^{+4} and attenuating the defects associated with Ce^{3+}. As the Ce^{3+}/Ce^{4+} ratio decreases, a decrease in the bond length and an increase in crystallinity are expected. The higher visibility of peak (222) at 600 °C may be related to the increase in oxide crystallinity with the annealing temperature [24]. It can also be observed in Figure 1 that new, low-intensity diffraction peaks appeared in the photoanode annealed at 600 °C, corresponding to signals from the substrate (FTO). This suggests that from this annealing temperature onward, the cracking of the oxide layer results in the formation of gaps between the aggregates, exposing the substrate, as displayed in the SEM image in Figure 1.

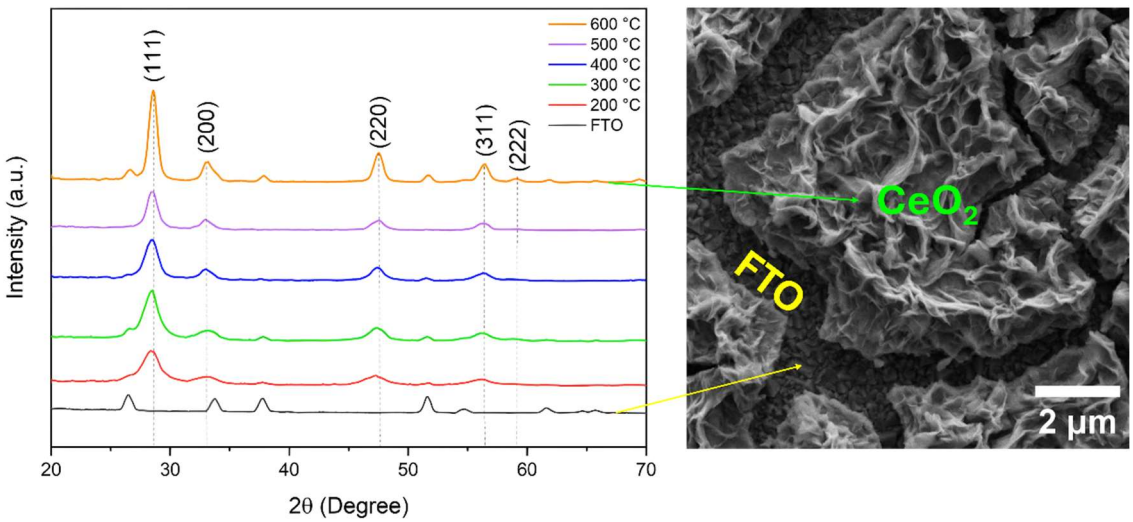

Figure 1. X-ray diffraction (XRD) spectra of CeO_2/FTO photoanodes annealed at different temperatures. The SEM micrograph shows the cracking of the layer and the exposure of the FTO substrate on CeO_2 annealed at 600 °C.

Table 1. Full width at half maximum (FWMH), crystallite size, and lattice parameter data from XRD. Peak area ratios (A_{Ce3+}/A_{Ce4+}) from Raman analysis of CeO_2 layers on FTO annealed at different temperatures are shown.

Temperature (°C)	FWMH (°)	Crystallite Size, D (nm)	Lattice Parameter, *a* (A°)	A_{Ce3+}/A_{Ce4+}
200	2.25	4.41	5.43	0.072
300	1.74	5.05	5.43	0.047
400	1.40	6.22	5.42	0.024
500	1.10	7.40	5.42	0.015
600	0.78	9.74	5.40	0.0090

Diffractograms were used to evaluate the effect of annealing temperature on the grain boundaries of CeO_2 at the nanocrystalline scale by determining the crystallite size (D) using Equation (12) [20].

$$D = 0.89\lambda/(\beta cos\theta) \quad (12)$$

Here, λ is the wavelength of X-ray radiation, β is the full width at half maximum for the diffraction peak with more intensity (111), and θ is the diffraction angle. The results reveal that the grain size of CeO_2 (D) increases with an increasing annealing temperature, which is consistent with observations from other studies. For instance, Jakub Ederer et al. [25] identified an increase in the crystallite size, pore volume, and surface area of CeO_2 obtained from carbonate salt after increasing the annealing temperature from 300 up to 700 °C. Jiang Liu [26] et al. also noted an increase in the crystallite size of CeO_2 with an increasing annealing temperature and attributed this to the non-uniform growth of the CeO_2. In general, the growth of CeO_2 crystallites may involve the aggregation of neighboring grains, a phenomenon explained by the fact that increasing the annealing temperature facilitates the combination of adjacent grains. Therefore, it is reasonable to expect that at higher annealing temperatures, grain boundaries are reduced and the electron mobility in CeO_2 is improved by reducing the number of trapping sites.

To evaluate the degree of distortion (strain) of the crystal lattice, the lattice constant *a* of CeO_2 was calculated as follows 13 [27]:

$$a = \frac{\lambda}{2sin\theta}\sqrt{h^2 + k^2 + l^2} \quad (13)$$

Here, θ is the Brag angle; h, k, and l are the Miller indices determined from each XRD pattern. The red graph in Figure S3 and the values in Table 1 illustrate the decrease in the lattice constant while increasing the annealing temperature of the CeO_2 photoanodes. Lattice constant values calculated for all photoanodes in this study agreed with previously reported values. The observed decrease was indicative of a slight shrinkage of the CeO_2 unit cell, which may have been due to the increased exchange of oxygen as the annealing temperature was raised. As mentioned above, cerium oxide exists in two forms, CeO_2 and Ce_2O_3, with the former having a higher oxygen content. The reaction between cerium oxide species and oxygen is as follows:

$$2CeO_2 \leftrightarrow Ce_2O_3 + \frac{1}{2}O_2 \quad (14)$$

Since the annealing in this study was performed in an uncontrolled atmosphere, the presence of oxygen in the furnace was significant, which shifts Reaction (13) to the left, favoring the more oxidized form (CeO_2). Therefore, as a higher temperature is expected to increase oxygen diffusion, the more compact and fluorite-like crystalline structure of $CeO)_2$ will be promoted. In addition, the decrease in the atomic radius (0.097 nm for Ce^{4+} versus 0.114 nm for Ce^{3+}) leads to the contraction of the oxide crystal structure. The decrease in *a* is significantly higher from 500 to 600 °C, possibly related to the higher conversion to Ce^{4+} and removal of impurities from the lattice. In summary, increasing the annealing

temperature leads to a compaction of the oxide structure by favoring the formation of Ce^{4+} in the lattice. The specific changes in crystalline properties at a given annealing temperature depend on the atmosphere in which the heating takes place.

3.2.2. Raman Spectroscopy

The chemical structure of the CeO_2 layers was evaluated using Raman spectroscopy to assess the effects of annealing temperature. Figure 2A displays both the Raman spectra of the electrodeposited CeO_2 annealed at various temperatures as well as that of the FTO substrate. The differences in the spectra compared to that of the substrate show that the CeO_2 layer was successfully deposited in all cases. In all spectra, a strong peak around 472 cm^{-1} was observed, corresponding to the Ce-O-Ce vibrational mode characteristic of the fluorite structure of CeO_2 in space group *Fm3m* [28]. The intensity of this peak increased strongly with the annealing temperature, indicating a larger structural order with heating. In addition, this peak showed a shift towards a higher wavenumber (blue shift) with an increasing annealing temperature, which is also typically associated with a higher structural order of the CeO_2.

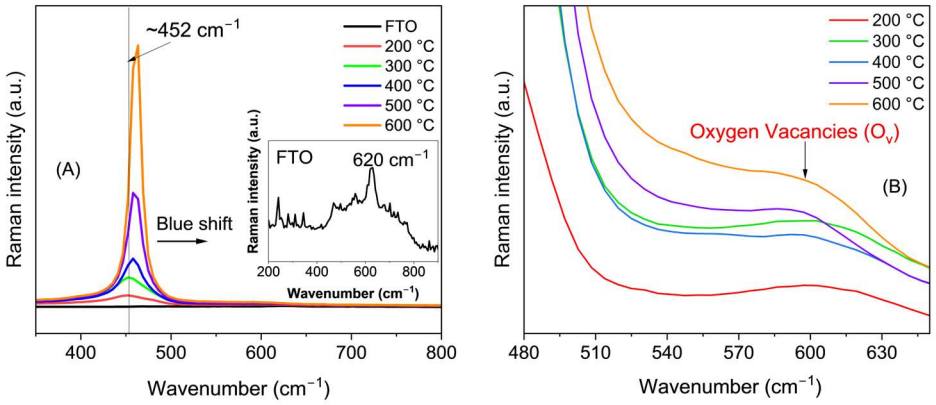

Figure 2. (**A**) Raman spectra of CeO_2 photoanodes obtained by electrodeposition on FTO and annealed at different temperatures. (**B**) Enlargement of the Raman peak at 600 cm^{-1}.

An analysis of defects in CeO_2 was conducted using Figure 2B. CeO_2 exhibited a small shoulder near 600 cm^{-1}, which could be attributed to the presence of oxygen vacancies associated with Ce^{3+} cations [27]. This signal was observed in all photoanodes, and its area decreased with an increasing annealing temperature, indicating a reduction in the relative concentration of Ce^{3+} in the material. As the Ce^{3+} concentration decreases, the number of defects and oxygen vacancies also diminishes.

The defect concentration in the CeO_2 photoanodes was estimated using the method purposed by Luo M-F in which the area ratio $A_{600}A_{472}$ (A_{Ce3+}/A_{Ce4+}) is calculated from Raman spectra [29]. These areas are recorded in Table 1 for the photoanodes annealed at different temperatures. All photoanodes contained lattice defects detectable by this technique, as indicated by the area values for the 600 cm^{-1} peak. It can be observed that the area under the peak at 472 cm^{-1} increased strongly with the annealing temperature while the area under the peak at 600 cm^{-1} showed much smaller variations. As a result, the ratio of the areas decreased with an increasing annealing temperature. This could indicate that increasing the annealing temperature enhances the ordering of the lattice due to the increase in the crystallite size, which is also suggested by the XRD results.

Area ratio estimation provides an approximation of the relative concentration of cerium species; however, it is important to consider the limitations of this approach. The main limitation is that there are likely to be combined contributions to the intensity of the Raman signals. For example, Schilling et al. compared the experimental Raman spectra of polycrystalline CeO_2 with the Raman spectra obtained from an ab initio density functional theory (DFT) study for CeO_2, and they found that octacoordinated Ce^{4+} and

six-coordinated Ce^{3+} centers can be responsible for the main peak at 470 cm^{-1}. Similarly, the signal around 600 cm^{-1} depends not only on Ce^{3+} but also on other cations [30]. In the study carried out here, the Sn atoms in the substrate may have diffused into the CeO_2 film at high temperatures; Sn in the lattice of CeO_2 could generate oxygen vacancies and may have contributed to the Raman peak at 600 cm^{-1}. Despite this limitation, it has been shown that this method can provide a good estimate of the Ce species composition in CeO_2.

3.2.3. XPS

The presence of cerium states (Ce^{4+}, Ce^{3+}) in the CeO_2 coating annealed at 600 °C was evaluated by X-ray photoelectron spectroscopy (XPS) measurements. Figure 3A shows the XPS survey spectrum, revealing O1s peaks corresponding to oxygen in the oxide lattice, Ce3d peaks associated with cerium species, and a signal at 284 eV related to C, likely due to CO_2 capture during the annealing process [31]. The peaks corresponding to Ce3d were deconvoluted and the signals were assigned according to Figure 3B. The sets of peaks were labelled as *u* and n, assigned to the spin–orbit doublets of Ce $3d_{3/2}$ and Ce $3d_{5/2}$ energies from 915 to 881 eV. The characteristic peaks denoted by u′ and ν′ at 902 and 882 eV, respectively, corresponded to the two final states of Ce^{3+} ions. Conversely, those marked by u, u^0, ν, u″, u‴, and ν‴ at 899, 898, 881, 907, 915, and 887 eV, respectively, were also associated with the three final states of Ce^{4+} ions. The peak denoted by u‴, associated with the Ce $3d_{3/2}$, was the fingerprint of the Ce^{4+} state in all samples. Based on the information provided, it can be concluded that the samples exhibited both Ce^{3+} and Ce^{4+} oxidation states for Ce ions [32].

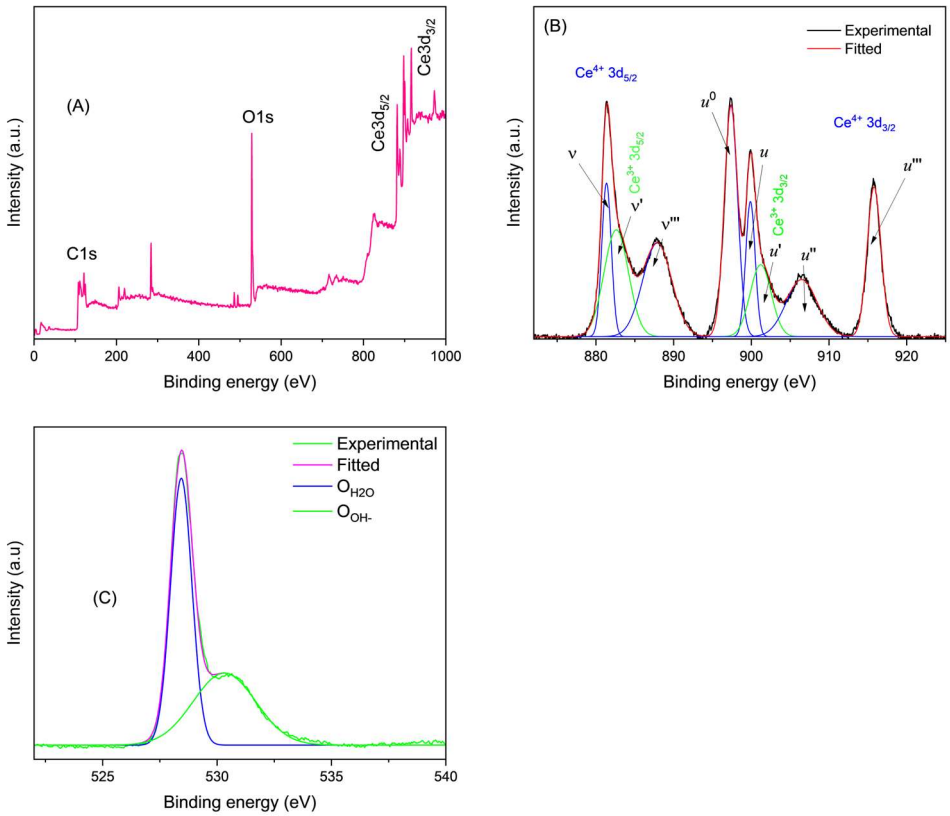

Figure 3. XPS spectrum of CeO_2 photoanode annealed at 600 °C: (**A**) survey spectrum; (**B**) Ce 3d, deconvoluted; (**C**) O 1 s, deconvoluted.

In addition to the Ce 3d signals corresponding to Ce^{3+} and Ce^{4+} centers, the O 1s peak was deconvoluted into two peaks at 528.4 and 530.6 eV (Figure 3C). The first and more intense peak at 528.4 eV corresponded to oxygen in the CeO_2 lattice (O_L) while the broader and less intense peak at 530.6 eV may have been associated with the irreversible adsorption

of water and the formation of surface hydroxyl groups following water dissociation. Several studies have attributed this signal to the presence of oxygen vacancies; however, this remains a controversial point as it is not possible to obtain a photoelectron signal from a non-existent atom [33–35].

Additionally, signals attributed to impurities, such as CO_2, can appear within this binding energy range, further complicating the accurate assignment of contributions to the O 1s peak. The difference in FWHM between the two peaks can be explained by the O_L signal being associated with a more uniform chemical environment, leading to a sharper, more defined binding energy. In contrast, the second peak, related to surface species, tended to show greater variability due to differences in adsorption sites [33].

3.3. SEM Analysis

Scanning electron microscopy (SEM) was used to evaluate the microstructures of CeO_2 layers electrodeposited on FTO and annealed at different temperatures (Figure 4). Firstly, the micrograph of the FTO substrate is shown, and the modification it underwent when the CeO_2 layers were deposited is clear. Moreover, SEM images show that for $Ce(OH)_3$ and CeO_2 at 200 °C, the microstructure of the layer was largely uniform. Between 300 °C and 600 °C, the cracking in the material was noticeable; the microstructure was irregular, rough, and clean, with ridges perpendicular to the surface, forming a porous sponge-like structure. This agreed with what is typically observed with CeO_2 deposits, which are characterized by being extremely rough layers.

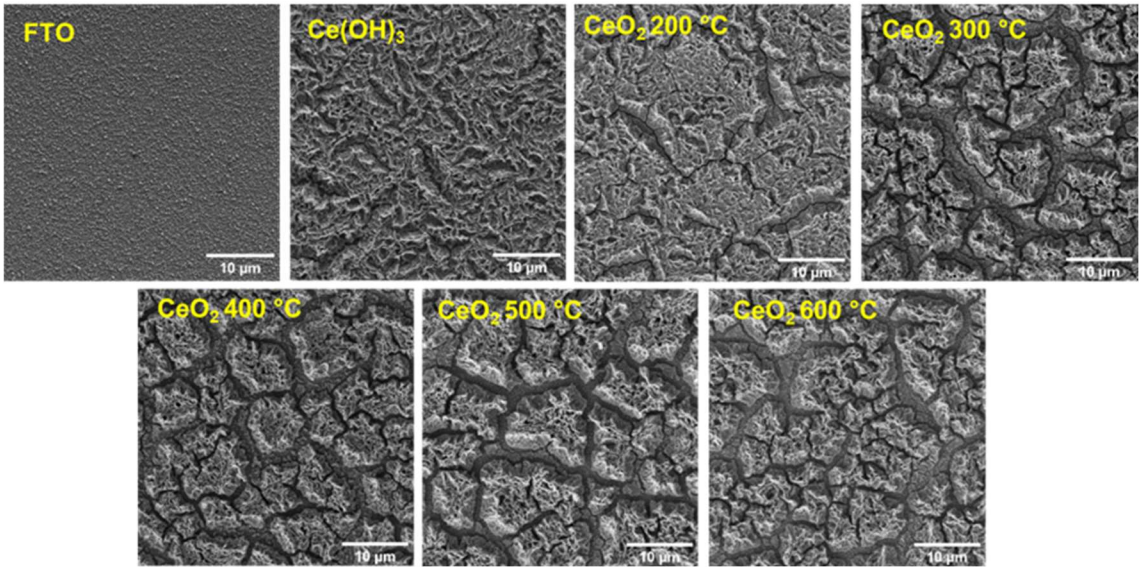

Figure 4. SEM images of CeO_2 photoanodes electrodeposited on FTO and annealed at different temperatures.

It can also be observed that at 300 °C, the shrinkage of the ridges was accentuated, leading to the formation of interstitial pores and more cracked zones. As the temperature reached 400 °C, 500 °C, and 600 °C, this phenomenon intensified, leading to pore consolidation and the formation of additional cracks. The cracks in this material were related to the volume changes induced by the conversion of hydroxide to CeO_2. They were also attributed to the difference in linear thermal expansion coefficients between the CeO_2 and the substrate, as well as to the loss of water incorporated into the material. Generally, cracking has been observed to negatively affect the long-term durability and functionality of the photoanode, and therefore, several strategies are being explored to relieve the stress and mitigate the cracking of CeO_2. For example, N. Ahmadizadeh et al. found that the electrodeposition of CeO_2 at a temperature slightly above 45 °C reduced the percentage of oxide cracking [36]. Other strategies to reduce cracking include the use of benzotriazole

salts or polymers during synthesis [37] and carrying out the electrodeposition in the presence of a surfactant [38]. In summary, the micrographs reveal the formation and separation of boundaries between aggregates caused by the increase in the annealing temperature. This segmentation is likely to cause changes in carrier mobility along these boundaries.

Cross-sectional images of the annealed coatings at different temperatures were also taken to estimate their thickness (Figure S4). From these images, the average thickness (n = 10) of each coating was estimated, including that of the unannealed $Ce(OH)_3$ composite; these values are presented in Table S1. Based on these values, it is noticeable that an increase in temperature leads to a decrease in the coating thickness, which is a known phenomenon due to a combination of causes [39]. One of the main reasons is that higher temperatures are more favorable for the evaporation of volatile compounds such as water or organic residues. Dehydration during annealing is a step involved in the conversion of $Ce(OH)_3$ to CeO_2, resulting in a more compact and thinner coating. Higher temperatures also promote a more pronounced sintering and densification of the material, helping the particles within the coating become more cohesive. Additionally, as the temperature increases, the coating may lose porosity due to pore collapse, making it denser. The sum of these causes results in a thinner CeO_2 layer as the annealing temperature increases.

3.4. Effect of Annealing Temperature on the Optical Properties of CeO_2 Photoanodes

Figure 5A shows the absorption spectra of CeO_2 photoanodes annealed at different temperatures compared to the absorption spectrum of the FTO substrate. The spectra indicate that all CeO_2 coatings exhibited absorption bands of significantly higher intensities than those of the substrate. It was observed that all photoanodes absorbed at wavelengths below 400 nm in the UV region, with multiple absorption bands related to multiple electronic transitions in the material. These bands corresponded to electronic transitions from valence bands in the CeO_2 between O2p orbitals and partially filled Ce4f orbitals and O2p orbitals and empty Ce4f orbitals [40]; another possible electronic transition in CeO_2 involves Ce5d orbitals [41].

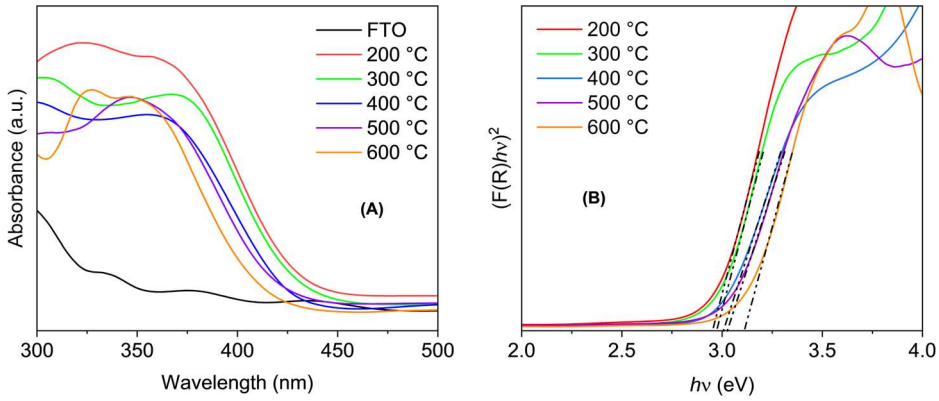

Figure 5. (**A**) Absorption spectra for CeO_2 photoanodes electrodeposited on FTO and annealed at different temperatures. (**B**) Tauc plots of CeO_2 photoanodes electrodeposited on FTO and annealed at different temperatures.

The electronic transitions of CeO_2 are related to the relative concentration of the Ce species in the oxide. According to the XRD and Raman results, it was observed that increasing the annealing temperature caused the amount of Ce^{+4} to increase with respect to Ce^{3+}. The small concentration of Ce^{3+} in the lattice could not only affect the absorption intensity of the UV-Vis spectrum of the oxide but also increase the number of transitions allowed in the band structure [42]. The existence of these intermediate states could be advantageous for the use of CeO_2 as a photoanode since it could improve light absorption and favor the separation of charges formed when the material is irradiated. It should be noted that the

absorption bands of the FTO substrate may have interfered with those of CeO_2 due to the cracking of the layers, particularly with an increasing annealing temperature (Figure 5A).

Variations in the coating thickness observed in the cross-sectional SEM images (Figure S4, Table S1) may have affected the light absorption of CeO_2. The higher thickness observed at lower annealing temperatures, associated with lower coating compaction, may have caused light scattering effects, such as multiple internal reflections, which increased the effective optical path length and thus increased absorption. However, further studies characterizing the porosity of the coating as a function of annealing temperature are needed to draw more definitive conclusions.

The direct optical band gap energy (E_g) values of CeO_2 photoanodes were determined from UV-Vis diffuse reflectance spectra. The Tauc equation was used to estimate the E_g values of CeO_2 photoanodes annealed at different temperatures (Equation (15)).

$$\left(F(R_\infty)\cdot h\nu\right)^{\frac{1}{\gamma}} = B\left(h\nu - E_g\right) \quad (15)$$

Here, B is a constant, h is the Plank constant, and n is the frequency. We have plotted the function $(F(R_\infty)\cdot h\nu)^{\frac{1}{\gamma}}$ on the y-axis and "hν" on the x-axis, with $\gamma = 2$ for a direct gap semiconductor [43]. Taking the linear section of each spectrum, the intercept with the x-axis corresponds to the optical band gap for each CeO_2 photoanode. The plots are shown in Figure 5B and the values for E_g at each temperature are listed in Table 2. The E_g values obtained are like those reported in the literature for CeO_2 [44], and it was observed that E_g increased with an increasing annealing temperature, from 2.96 eV (200 °C) to 3.12 eV (600 °C), which could have been related to the increase in the crystallite size.

Table 2. Band positions (vs NHE) of CeO_2 photoanodes annealed at different temperatures. The band gap (E_g) was calculated from Tauc plots in Figure 5B.

T(°C)	E_g (eV)	E_{CB} (eV)	E_{VB} (eV)
200	2.96	−0.42	2.54
300	2.98	−0.43	2.55
400	3.02	−0.45	2.57
500	3.05	−0.46	2.59
600	3.12	−0.50	2.62

Using the estimated values for E_g, the energy of the conduction band (E_{CB}) and the energy of the valence band (E_{VB}) were calculated using Equations (16) and (17) [45]:

$$E_{CB} = \chi - E_e - 0.5E_g \quad (16)$$

$$E_{VB} = E_g + E_{CB} \quad (17)$$

Here, χ is the absolute electronegativity of the semiconductor (5.56 eV for CeO_2) and E_e is the energy of the free electrons in the hydrogen scale (4.5 eV) [46]. The obtained values for E_{CB} and E_{VB} are shown in Table 2, which indicates that as the annealing temperature of CeO_2 increases, E_g increases and E_{CB} and E_{VB} splitting occurs. This behavior in the band structure of CeO_2 can be related to the decrease in lattice constant with an increasing annealing temperature (Figure S3), causing the atoms to be closer together and the electrons to be more tightly bound to the atoms. As a result, more energy is required to excite the valence band electrons, causing the band gap to increase. This observation is consistent with the results of Acosta-Silva et al., [19] who proposed that the broadening of the band gap is caused by reductions in the ionic size and increases in the crystallinity of CeO_2. Through structural characterization, they observed that the annealing temperature affects the stoichiometry of the oxide and thus the generation of intermediate energy levels associated with oxygen vacancies [40]. The existence of intermediate levels between VB and CB resulting from oxygen vacancies and partially filled 4f orbitals is also likely, and

these levels may act as electron trapping centers, thereby enhancing charge separation. These levels can be seen in the UV-Vis spectrum of CeO_2, where several transitions are observed (Figure 5A).

3.5. Photoelectrochemical Properties of CeO_2 Photoanodes

The photoelectrochemical performance of CeO_2 layers on FTO as photoanodes was evaluated by linear scanning voltammetry (LSV) and chronoamperometry (CA) in 0.1 M Na_2SO_4 in the presence of oxygen. When CeO_2 absorbs light photons with an energy higher than its E_g, electronic transitions from the valence band to the conduction band occur, generating charge carriers (electrons and holes) in the material. The efficient separation of these carriers and proper alignment of the energy levels of the photoanode and the species in solution facilitate an interfacial oxidation reaction involving the generated holes. At potentials above 1.4 V vs. RHE, the photoelectrochemical oxidation of water via the oxygen evolution reaction (OER) on the CeO_2 surface and the oxidation from Ce^{3+} to Ce^{4+} could contribute to the total photocurrent under light conditions. These photoelectrochemical processes involve the direct or indirect production of reactive oxygen species on the surface of the photoanodes. Figure 6 shows the linear sweep voltammetry (LSV) results of CeO_2 photoanodes as a function of annealing temperature, obtained in a potential window of 1.1 to 1.8 V (vs. RHE) under chopped light in 0.1 M Na_2SO_4. The current steps correspond to the photocurrents (J) generated by the oxide layer when exposed to illumination. This current behavior in light and dark conditions confirms that the material has photoanode properties as the electronic transition, the generation of charge carriers (electron–hole), and their effective separation are present for the redox chemical reaction to occur. The LSV plots show that the photocurrents produced by the CeO_2 photoanodes differed from that produced by the FTO substrate, with the photocurrents increasing with the oxide annealing temperature and reaching a maximum value of about 1.15 $\mu A/cm^2$ at 1.18 V for a temperature of 600 °C. This behavior could have been related to the increase in the crystallite size (D); the larger the D value is, the fewer grain boundaries there will be, which will reduce the resistance to carrier flow and increase the photocurrent. This agrees with the XRD characterization, where it was found that an increase in the annealing temperature of the CeO_2 coating improves its crystallinity and potentially reduces grain boundaries (Figure S3). Likewise, the Raman characterization showed a progressive ordering of the structure with an increasing annealing temperature, which would increase the mobility of electrons in the CeO_2 lattice, thereby increasing the photocurrent.

Another critical factor affecting the performance of photoanodes is the stability of the photocurrent over time. To evaluate this parameter, chronoamperograms of the photoanodes were prepared at 1.8 V (vs. RHE) in a 0.1 M Na_2SO_4 solution under chopped light (100 mW/cm^2). Similar to the LSV results, the chronoamperograms in Figure 7 verify the photoactivity of the electrodes and show higher photocurrents as the oxide annealing temperature increased. It was also observed that the photocurrents of the CeO_2 photoanodes were noticeably higher than the photocurrent of the FTO substrate.

Figure 7 also shows differences in the recombination photocurrent for each step as the annealing temperature of the photoanodes was varied, which corresponded to the delta between the start (J_A) and end (J_B) points of the photocurrent. Similarly, it was observed that the total change in the photocurrent at the electrodes (ΔJ_{Total}), calculated as the delta between the end point of the last photocurrent step and the end point of the first step, varied with the annealing temperature (Table S2). Based on the values from ΔJ_{total}, the photocurrents of the photoanodes annealed at the highest temperatures (500 °C and 600 °C) were the least stable as they showed the largest decrease during the 300 s. The same photoanodes had the highest recombination photocurrents; this behavior has been observed by others and is attributed to the recombination of charge carries, charge accumulation on the photoanode surface, and the irreversible adsorption of sulfate anions present in the supporting electrolyte [47]. One factor that could have favored the accumulation of

charge on the oxide surface was the increase in the cracking of the material as the annealing temperature increased.

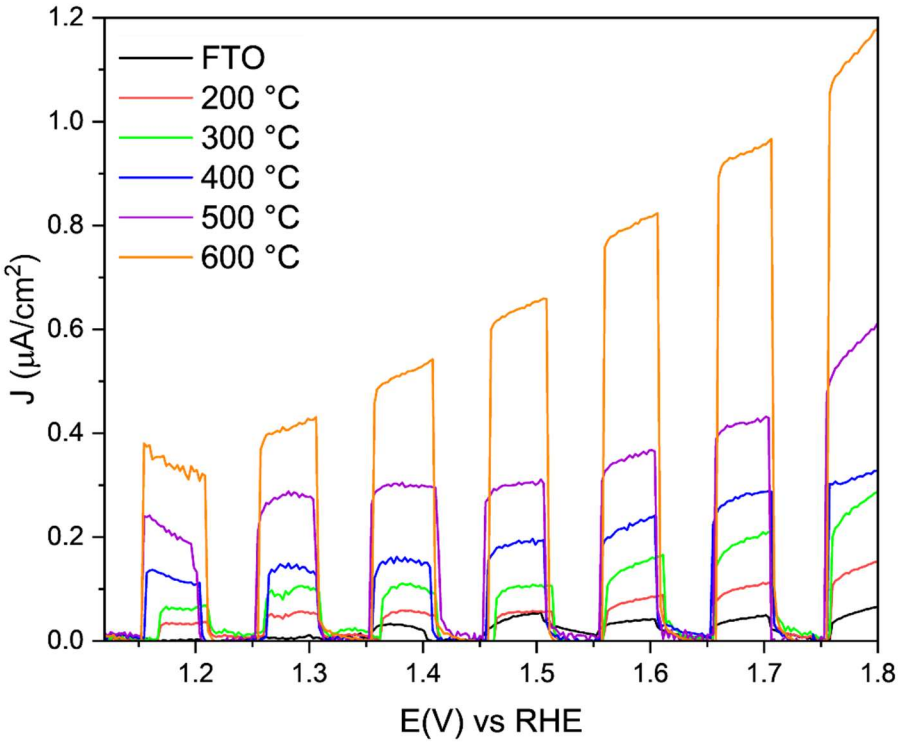

Figure 6. LSV of CeO_2 photoanodes obtained by electrodeposition and annealed at different temperatures. Measurements were performed from 1.11 to 1.8 V (vs. RHE) at 10 mV/s in a 0.1 M Na_2SO_4 solution. Chopped light was used (100 mW/cm^2).

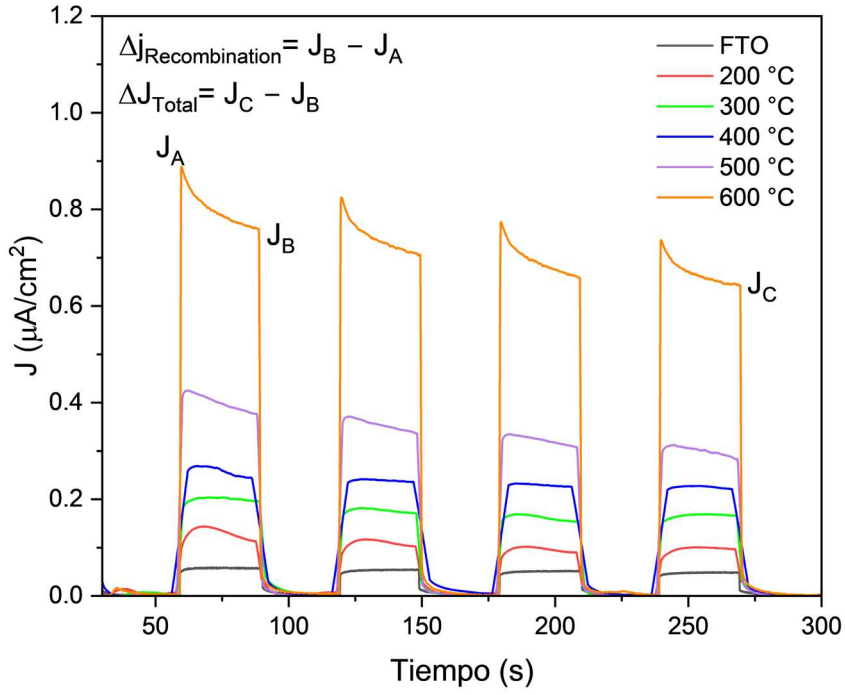

Figure 7. Chronoamperometries of CeO_2 photoanodes obtained by electrodeposition and annealed at different temperatures. The measurements were performed at 1.8 V (vs. RHE) for 300 s in a 0.1 M Na_2SO_4 solution. Chopped light was used (100 mW/cm^2).

Table 3 shows the photocurrents obtained in this and other studies evaluating the photoelectrochemistry of various CeO_2-based compounds under different electrolytes and radiation conditions. Although it is not possible to directly compare the photocurrents due to the variety of measurement conditions, it was observed that the CeO_2 layers in this study (annealed at 600 °C) reached similar values to those of other CeO_2-based photoelectrodes. Since this photoanode produced the highest value of photocurrent, it can be assumed that for this system (CeO_2/FTO), 600 °C is the optimum annealing temperature of the oxide in an air atmosphere. However, as mentioned above, it is important to note that at this temperature, the cracking of the oxide layer is also intensified. In the future, it would be advisable to study modifications of the synthesis medium to help prevent cracking, such as those proposed in [39,40].

Table 3. Photocurrent densities produced by CeO_2-based photocatalysts.

System	Light Source	J (mA/cm^2)	Conditions	Ref
CeO_2—1000 °C	(AM) 1.5 filter	0.22	Bias potential: 0.0 V vs. Ag/AgCl	[48]
CeO_2-g-C_3N_4 QDs	300 W Xe lamp	0.70	Na_2SO_4 0.5 M	[49]
CeO_2-g-Ag QDs	300 W Xe lamp	0.50	Bias potential: 1.0 V SCE	[50]
CeO_2-g-C_3N_4	500 W Xe lamp	0.35	Na_2SO_4 0.1 M	[51]
CeO_2 nanorods	500 W Xe lamp	1.20	KOH 1.0 M + CH_3OH 1.0 M	[52]
ITO-CeO_2-PDA-C	300 W Xe lamp	3.00	Na_2SO_3 0.2 M	[53]
NiO-CeO_2	125 W Hg lamp	5.50	Na_2SO_4 0.1 M	[24]
FTO-CeO_2/Cds	Blue LED lamp 470 nm	2.00	Na_2SO_4 0.1 M	[54]
FTO-CeO_2	(AM) 1.5 filter	1.20	Bias potential: +1.2 V vs. Ag/AgCl Na_2SO_4 0.1 M 1.8 V vs. RHE	This study

As a preliminary evaluation of the stability of the CeO_2—600 °C photoanode, a chronoamperometric measurement was performed for 1 h at 1.8 V vs. RHE in 0.1 M Na_2SO_4 under continuous illumination (Figure S5). This result indicated a rapid decay in photocurrent for approximately 600 s, followed by a slower decrease until 2400 s. After this point, the photocurrent stabilized at approximately 1.00 μA/cm^2 until the end of the measurement. One of the major causes of photoactivity loss in photoelectrodes is photocorrosion, which occurs as the material degrades due to continuous exposure to light and electrolyte. Another significant cause is surface passivation, characterized by the accumulation of reaction products that block active sites [47]. Addressing the factors that contribute to the loss of photoactivity is a critical research topic in photoelectrochemistry, with the most promising strategies including surface modifications, the doping of oxides, and the formation of heterojunctions [55].

In addition, the CeO_2—600 °C photoanode showed good reproducibility in the photoelectrochemical response when evaluated by chopped chronoamperometry (Figure S6). In this figure, the photocurrents generated by three CeO_2—600 °C electrodes in 0.1 M Na_2SO_4 at 100 mW/cm^2 for 300 s are observed. The three photoanodes showed similar behaviors: the current increased rapidly under illumination and dropped completely when the light was turned off. Moreover, the photocurrent values in successive cycles were comparable for the three photoanodes, indicating good reproducibility in the electro-optical and structural properties of the coating.

To investigate the charge transport on the interface CeO_2—electrolyte, electrochemical impedance spectroscopy measurements were performed in 0.1 M Na_2SO_4 solution at 1.0 V vs. Ag/AgCl (1.6 vs. RHE). Figure 8 shows the Nyquist plots obtained from impedance measurements of CeO_2 photoanodes annealed at different temperatures, including the plot corresponding to the FTO substrate. In a typical Nyquist plot, an arc at high frequencies and a straight line at low frequencies are observed. The diameter of the semicircular arc corresponds to the charge transfer resistance (R_{ct}) at the electrolyte–electrode interface [56].

In Figure 8, it is observed that the diameter of the semicircles corresponding to CeO_2 photoanodes tends to decrease with an increasing annealing temperature.

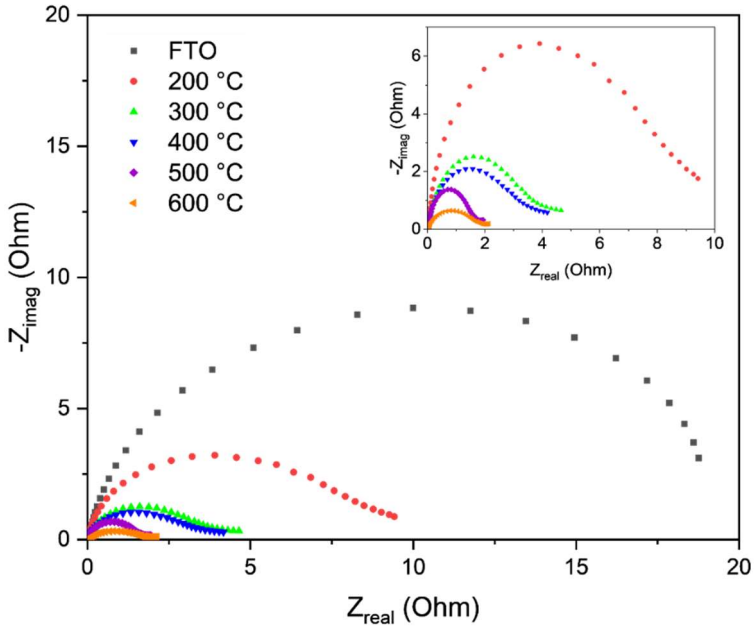

Figure 8. Nyquist plot of CeO_2/FTO photoanodes annealed at different temperatures. Measurements were performed in 0.1 M Na_2SO_4 from 0.1 Hz to 100 KHz at 1.8 V vs. RHE illumination (100 mW/cm^2).

To determine the charge transfer parameters of CeO_2 photoanodes, we used an equivalent circuit to model the electrolyte–CeO_2 interface (Scheme 1). This circuit yielded χ^2 values of 10^{-3}, suggesting a very good fit between the model of the photoelectrochemical system and the experimental data, and consequently, a minimal residual error between simulated and measured values. The model included a resistance representing the solution resistance (R_s) connected in series with a constant phase element (CPE), which modelled the double-layer capacitance (C_{dl}) at the electrolyte–CeO_2 interface. Finally, a second resistance represented the charge transfer resistance (R_{ct}) between the electrode and the solution interface [57]. Table 4 shows the fitted values of each of the parameters according to the equivalent circuits for the five CeO_2 photoanodes. It was observed that as the annealing temperature increased, the photoanode charge transfer resistance (R_{ct}) decreased. This trend could have been related to the larger and more defined crystallites in the CeO_2 microstructure at the higher annealing temperatures, which was consistent with the results observed by XRD (Figure S3, Table 1). This microstructural feature reduced the discontinuities that impeded charge transport, allowing the carriers to move more fluidly through the oxide with less likelihood of recombination. The R_{ct} behavior may also have been related to the thinner layer thickness as the annealing temperature increased. In a more compact microstructure, the charge transport paths may be shorter and more direct, resulting in less resistance to charge transport.

Table 4. Equivalent circuit parameters for CeO_2 photoanodes annealed at different temperatures. E_{fb} and N_D values were obtained from the Mott–Schottky plots in Figure 9 and Equation (19).

T (°C)	R_s (W/cm^2)	R_{ct} (W/ cm^2)	χ^2	E_{FB} vs. NHE (V)	N_D (cm^{-3})
200	37.5	4385	0.003	−0.48	5.9×10^{20}
300	39.5	3715	0.004	−0.30	5.5×10^{20}
400	36.9	3347	0.003	−0.11	7.8×10^{20}
500	36.5	1813	0.004	0.013	5.9×10^{20}
600	37.3	823	0.002	0.12	7.5×10^{20}

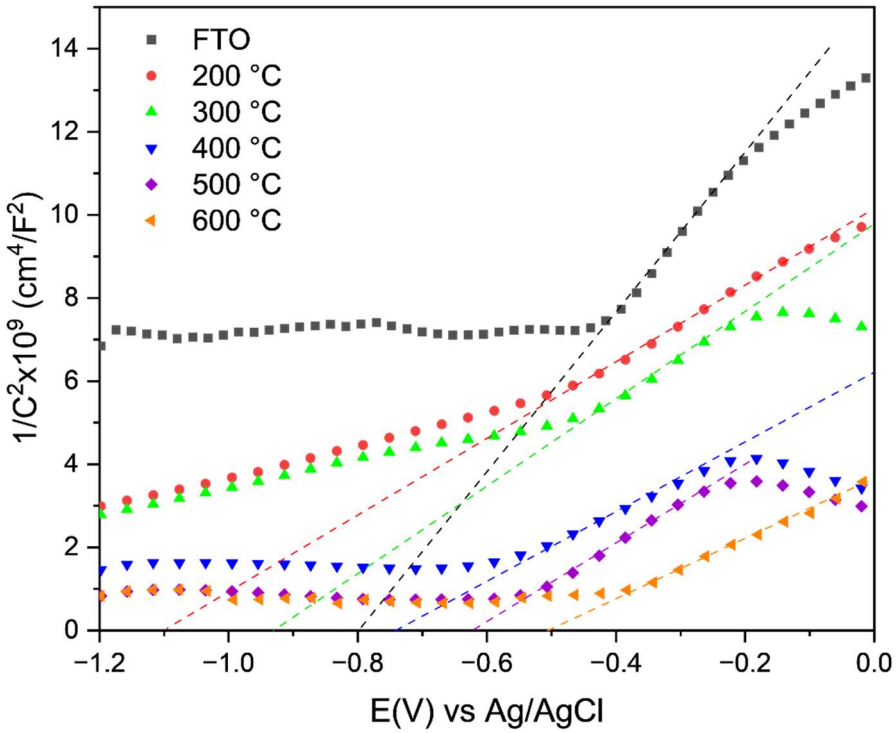

Figure 9. Mott–Schottky (M-S) diagrams of CeO_2 photoanodes annealed at different temperatures. EIS measurements were performed in 0.1 M Na_2SO_4 solution at 1000 Hz (−1.2 V to 0.0 V vs. Ag/AgCl) under illumination (100 mW/cm^2).

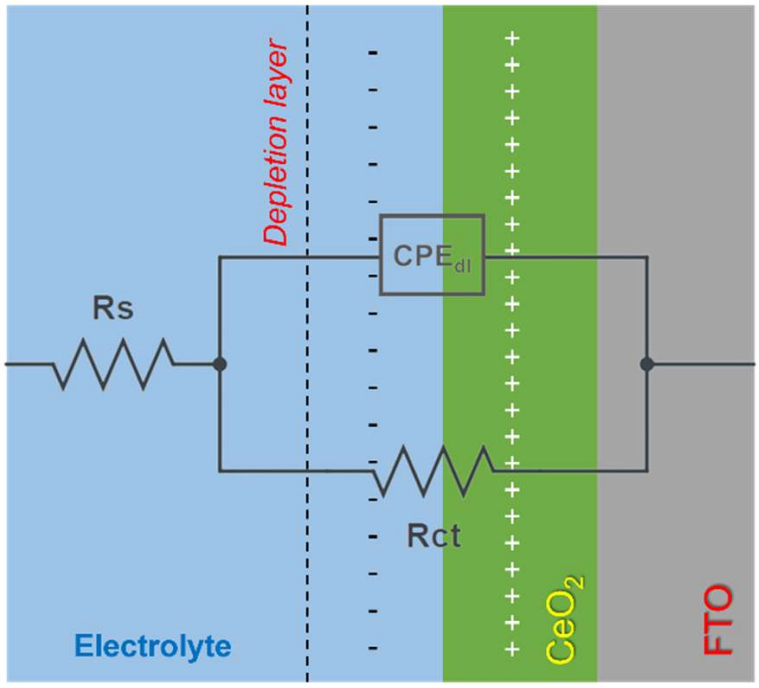

Scheme 1. Depletion layer created by charge transfer between the electrolyte and the CeO_2 layer on FTO. Equivalent circuit used to model the photoelectrochemical response by EIS. Based on reference [58].

In the equivalent circuit, the constant phase element (CPE) modelled the double layer at the interface. It considered factors that affected the ideal capacitance of the system, such as surface inhomogeneity, porosity, or the high roughness of the CeO_2 layer. Table 5

presents the CPE and n values for each photoanode. In all cases, n was approximately 0.9, indicating that the coatings exhibited highly capacitive behavior. Using the CPE values, the effective capacitances (C_{eff}) of the photoanodes were calculated with Brug's equation (Equation (18)) [59]. No clear trend was observed with annealing temperature, and all C_{eff} values were close to 1 μF (Table 5).

$$C_{eff} = \left(CPE \cdot R_{ct}^{1-n}\right)^{\frac{1}{n}} \quad (18)$$

Table 5. Calculation of effective capacitance using Brug's equation.

T(°C)	CPE ($mF \cdot s^{(n-1)}$)	n	C_{eff} 10^{-5} (F)
200	18.1	0.887	1.31
300	18.3	0.855	1.15
400	20.9	0.854	1.32
500	21.0	0.847	1.16
600	16.6	0.887	0.97

From the EIS measurements of the CeO_2–electrolyte interface, Mott–Schottky (M-S) plots were obtained to determine important operating parameters of photoelectrodes such as the flat-band potential (E_{fb}) and donor density (N_D). The plots were obtained from Equation (19):

$$\frac{1}{C^2} = \frac{2}{\varepsilon\varepsilon_0 N_D}\left(E - E_{fb} - \frac{k_B T}{q}\right) \quad (19)$$

Here, C is the capacitance; ε and ε_0 are the dielectric constant of the semiconductor (for CeO_2 was reported a value of 26) [60] and the vacuum permittivity (8.85×10^{-12} F/m), respectively; E is the applied potential; k_B is Boltzmann's constant; T is the temperature; and q is the charge of the electron (1.60×10^{-19} C). By taking the central linear portion of the M-S graph and plotting the line in the x-axis where $1/C^2 = 0$, the flat-band potential vs. Ag/AgCl is estimated and can be converted to the normal hydrogen electrode (NHE) scale.

Figure 9 shows the Mott–Schottky plots for the CeO_2 photoanodes. In all cases, a linear section with positive slope is observed, even with the FTO substrate. The positive slope in this plot is an indication that the material exhibits N-type behavior [61]. The values of the flat-band potential (E_{fb}) vs. the normal hydrogen electrode (NHE), together with the donor density (N_d) for each photoanode, are listed in Table 4. The E_{fb} values shifted towards anodic values as the annealing temperature increased; this shift may have been related to an increase in the concentration of minority charge carriers in the depletion layer caused by rapid charge separation [61]. It should be noted that the interaction of charge carriers with adsorbed species or surface defects of CeO_2 can alter the charge distribution and affect the E_{fb}. Annealing can cause the formation and removal of defects in the oxide, which can influence the generation, recombination, and mobility of the carriers. Similarly, annealing impacts the morphology of the oxide, which in turn affects its interaction with the electrolyte and potential adsorbates.

The donor density (N_d) in CeO_2, related to the oxygen vacancies in the lattice, shows no trend with annealing temperature according to the values calculated from Equation (19) (Table 4). However, as discussed earlier, Raman analysis suggests a decrease in oxygen vacancies with an increasing annealing temperature due to the decrease in the Ce^{3+}/Ce^{4+} ratio. Nevertheless, it is important to consider that the N_d value is not only influenced by the oxygen vacancy concentration but also by a combination of factors such as exposure to reactive species, geometrical parameters, and layer morphology. Additionally, negative slopes are observed in the Mott–Schottky plots beyond −0.2 V vs. Ag/AgCl for photoanodes annealed at 300 °C, 400 °C, and 500 °C. These negative slopes are attributed to the partially positive character (p-type behavior) of the CeO_2 photoanodes [62].

3.6. Electronic Band Structure of CeO_2 Photoanodes

The energy band structure for CeO_2 is presented in Scheme 2, which was made using the E_g results from the Tauc plots and the E_{fb} values from the EIS measurements. According to the band structure diagram, the valence and conduction bands are located at +2.54 eV and −0.42 eV (200 °C), +2.55 eV and −0.43 eV (300 °C), +2.57 eV and −0.45 eV (400 °C), +2.59 eV and −0.46 eV (600 °C), and +2.62 eV and −0.50 eV (600 °C). The diagram also shows the estimated positions of the Fermi level for the photoanodes (−0.48 eV (200 °C), −0.30 eV (300 °C), −0.11 eV (400 °C), 0.013 eV (500 °C), and 0.12 eV (600 °C)). According to the literature, the valence band of CeO_2 corresponds to O2p orbitals and the conduction band to partially filled Ce4f orbitals due to Ce^{3+} ($Z[Ce^{3+}] = 5s^25p^64f^1$), with a theoretical band gap of 3.0 eV [63]. According to the UV-Vis characterization, mid-gap levels are likely to be formed by empty Ce4f orbitals of Ce^{4+} ($Z[Ce^{4+}] = 5s^25p^64f^0$). Thus, although E_g increases slightly with the annealing temperature, the mid-gap states could facilitate the electron transition and thus the photoelectrochemical performance of the annealed photoanodes at higher temperatures.

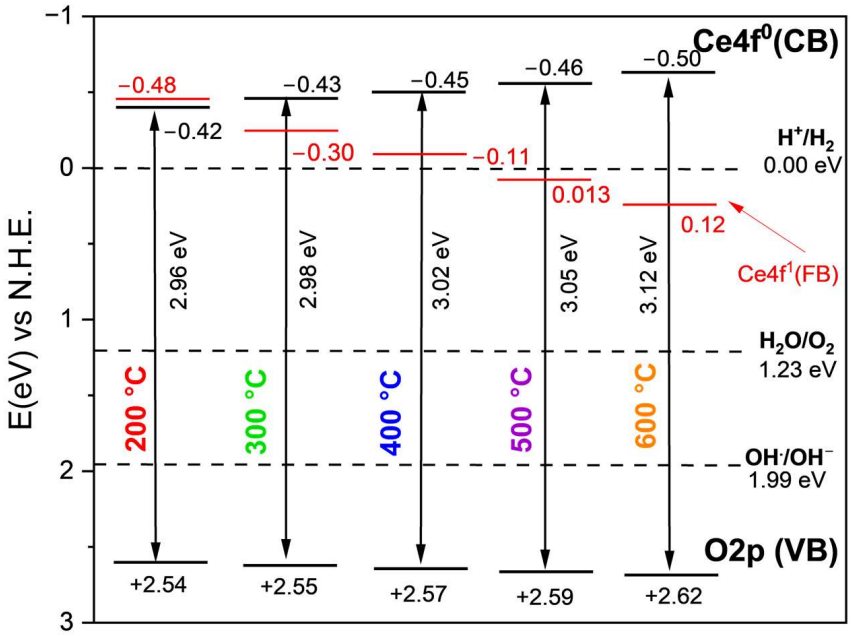

Scheme 2. Electronic band structure of CeO_2 photoanodes obtained by electrodeposition on FTO at different annealing temperatures.

The position of the energy levels in a semiconductor material plays a critical role in its potential photocatalytic applications. Variations in the energy band can cause changes in the material's ability to absorb light of certain wavelengths, as well as in the efficient formation and separation of electron–hole pairs. In addition, the proper positioning of the energy levels with respect to the redox potentials of the analytes is essential in the photocatalytic process. Therefore, the effects we observed of the annealing temperature on the oxide's band structure are important in determining the feasibility of CeO_2/FTO in the photoelectrocatalysis of molecules of interest.

The higher photocurrent density obtained with the photoanode annealed at 600 °C can be attributed to a combination of factors associated with an increasing annealing temperature, mainly higher crystallinity with fewer grain boundaries and significantly reduced charge transfer resistance. This interpretation aligns with findings by Wang et al., who observed improved photoelectrochemical performance for OER in $BiVO_4$ photoelectrodes at higher annealing temperatures (540 °C) due to enhanced charge transport efficiency [64]. In addition, the thinner thickness of the annealed coating at 600 °C may have an effect, as

recombination losses may be lower due to the shorter distance the carriers have to travel to reach the surface.

Thus, the results of this work will contribute to the design of CeO_2 photoanodes obtained by electrodeposition on conducting glass. It is common for semiconducting oxides to be combined with other materials to increase the photocurrent (Table 3); therefore, the findings of this study offer a better understanding for optimizing the electrosynthesis conditions of the base material. Regarding the energy levels of CeO_2, they are well suited for catalyzing reactions such as oxygen evolution and hydroxyl radical formation (Scheme 2). In this field of research, understanding these types of reactions using immobilized photoanodes, such as those developed here, is becoming increasingly interesting. This approach takes advantage of the ease of separation and reuse of the electrode, as well as of the greater penetration of radiation in the material compared to semiconductors in suspension.

4. Conclusions

The photoelectrochemical, optical, and structural properties of CeO_2 photoanodes obtained by electrodeposition on FTO substrates and annealed at different temperatures were investigated. Structural characterization showed that enhancing the annealing temperature of CeO_2 increases the order, density, and crystallinity of the oxide layers while decreasing the grain boundaries, which is beneficial for charge transport. The morphology of CeO_2 deposited on FTO showed ridges, voids, and cracks, and the coating became more compact with an increasing annealing temperature. The CeO_2/FTO electrodes showed photoactivity as anodes, and their photocurrent improved with a rising annealing temperature, with the best value being 1.15 $\mu A/cm^2$ at 1.8 V vs. RHE (600 °C). Photocurrent stability was acceptable for all photoanodes under the measured conditions, but recombination was more pronounced at higher annealing temperatures. The charge transfer resistance of the photoanodes decreased significantly with an increasing annealing temperature, contributing to the higher photocurrent measured by EIS. This characterization also confirmed that the oxides exhibit N-type behavior when evaluated down to −0.2 V (vs. Ag/AgCl) by M-S plots, which was consistent with the anodic shift of E_{fb} observed with an increasing annealing temperature. From the UV spectra, the band gap energy of CeO_2 was found to increase slightly with the annealing temperature. However, the probable formation of intermediate energy states favors the electronic transition, which may lead to the highest photocurrent presented by the photoanode annealed at the highest temperature (600 °C). Therefore, it has been shown that electrodeposition allows to obtain CeO_2/FTO photoanodes with electronic, optical, and structural properties that are influenced by the annealing temperature. Thus, annealing temperatures of 500 and 600 °C are the most attractive to take advantage of the photoelectrochemical activity of the electrode by producing the best photocurrent values.

Supplementary Materials: The following supporting information can be downloaded at: https://www.mdpi.com/article/10.3390/surfaces7040059/s1, in the beginning. Figure S1. Chronoamperometry for the electrodeposition of Ce-based photoanodes (−1.2 V vs. Ag/AgCl). The synthesis solution was 25 mM $CeCl_3$ and 50 mM $NaNO_3$ at pH 4.5. Figure S2. (A) $Ce(OH)_3$ electrodeposited on FTO substrate (immediately after electrosynthesis). (B) CeO_2 layer obtained after annealing at 600 °C. Figure S3. Changes in crystallite size and lattice constant (a) with annealing temperature of electrodeposited CeO_2 layers on FTO. Figure S4. SEM Cross-sectional images of coatings on FTO. $Ce(OH)_3$ layer was obtained by electrodeposition and CeO_2 was obtained from $Ce(OH)_3$ by annealing at different temperatures. Figure S5. Curve I-t of CeO_2 photoanode annealed at 600 °C. The measurements were performed at 1.8 V (vs. RHE) for 3600 s in a 0.1 M Na_2SO_4 solution. (100 mW/cm^2). Figure S6. Chopped photocurrent produced by CeO_2 photoanodes annealed at 600 °C. The measurements were performed at 1.8 V (vs. RHE) in a 0.1 M Na_2SO_4 solution and 100 mW/cm^2. Table S1. Average thicknesses of CeO_2 coatings on FTO annealed at different temperatures. Each mean value and its standard deviation were calculated from ten measurements taken from the cross-sectional SEM image of the coating. Table S2. Drops in the photocurrent (DJ) during each stage of illumination (steps). The CeO_2 photoanodes were obtained at different annealing temperatures.

Author Contributions: A.E.M.-L. conducted the experimental tests and edited the manuscript. M.T.C. and P.O. edited and reviewed the manuscript. M.R.V.L. contributed with the XPS measurement of the study material. The manuscript was written through the contributions of all authors. All authors have read and agreed to the published version of the manuscript.

Funding: This research was funded by Universidad de Los Andes, grant number Project INV-2021-118-2235.

Institutional Review Board Statement: Not applicable.

Informed Consent Statement: Not applicable.

Data Availability Statement: Data are contained within the article and the supplementary materials. Any additional data will be available upon request.

Acknowledgments: The authors thank the Department of Chemistry and the Department of Chemical Engineering for their support. M.T.C. thanks the Faculty of Science. A.M. thanks the Faculty of Science (Project INV-2021-118-2235). The authors acknowledge the instruments and scientific and technical assistance of the MicroCore Microscopy Core at the Universidad de Los Andes (vicepresidency for research and creation).

Conflicts of Interest: The authors declare no conflict of interest.

References

1. Fathima Khyrun, S.M.; Jegatha Christy, A.; Mayandi, J.; Sagadevan, S. Synergistic Effect of Nano-Floret CeO_2/ZnO Nanocomposite as an Efficient Photocatalyst for Environmental Remediation. *Ceram. Int.* **2024**, *50*, 11817–11832. [CrossRef]
2. Chibac-Scutaru, A.L.; Podasca, V.; Dascalu, I.A.; Melinte, V. Exploring the Influence of Synthesis Parameters on the Optical Properties for Various CeO_2 NPs. *Nanomaterials* **2022**, *12*, 1402. [CrossRef] [PubMed]
3. Ahmad, N.; Alghamdi, A.A.; Al-Abdulkarim, H.A.; Mustafa, G.M.; Baghdadi, N.; Alharthi, F.A. Structural, Morphological, and Electrochemical Performance of CeO_2/NiO Nanocomposite for Supercapacitor Applications. *Appl. Sci.* **2021**, *11*, 411. [CrossRef]
4. Alharthi, F.A.; Alanazi, H.S.; Abdullah Alsyahi, A.; Ahmad Citation, N.; Hydrothermal Synthesis, N.; Syrek, K.; Vergara, A. Hydrothermal Synthesis, Characterization and Exploration of Photocatalytic Activities of Polyoxometalate: Ni-$CoWO_4$ Nanoparticles Characterization and Exploration of Photocatalytic Activities of Polyoxometalate: Ni-$CoWO_4$. *Crystals* **2021**, *11*, 456. [CrossRef]
5. Mancuso, A.; Iervolino, G. Synthesis and Application of Innovative and Environmentally Friendly Photocatalysts: A Review. *Catalysts* **2022**, *12*, 1074. [CrossRef]
6. Jamkhande, P.G.; Ghule, N.W.; Bamer, A.H.; Kalaskar, M.G. Metal Nanoparticles Synthesis: An Overview on Methods of Preparation, Advantages and Disadvantages, and Applications. *J. Drug Deliv. Sci. Technol.* **2019**, *53*, 101174–101185. [CrossRef]
7. Yan, Z.; Liu, H.; Hao, Z.; Yu, M.; Chen, X.; Chen, J. Electrodeposition of (Hydro)Oxides for an Oxygen Evolution Electrode. *Chem. Sci.* **2020**, *11*, 10614–10625. [CrossRef] [PubMed]
8. Rebey, A.; Hamdi, R.; Massoudi, I.; Hammami, B. In Situ Electrodeposition of Pb and Ag Applied on Fluorine Doped Tin Oxide Substrates: Comparative Experimental and Theoretical Study. *Materials* **2022**, *15*, 8865. [CrossRef]
9. Orozco-Messana, J.; Camaratta, R. ZnO Electrodeposition Model for Morphology Control. *Nanomaterials* **2022**, *12*, 720. [CrossRef]
10. Pikalova, E.; Osinkin, D.; Kalinina, E. Direct Electrophoretic Deposition and Characterization of Thin-film Membranes Based on Doped $BaCeO_3$ and CeO_2 for Anode-supported Solid Oxide Fuel Cells. *Membranes* **2022**, *12*, 682. [CrossRef]
11. Zeng, Y.B.; Qu, N.S.; Hu, X.Y. Preparation and Characterization of Electrodeposited Ni-CeO_2 Nanocomposite Coatings with High Current Density. *Int. J. Electrochem. Sci.* **2014**, *9*, 8145–8154. [CrossRef]
12. Yang, Y.; Du, X.; Yi, C.; Liu, J.; Zhu, B.; Zhang, Z. Structural, Optical and Electrical Properties of CeO_2 Thin Films Simultaneously Prepared by Anodic and Cathodic Electrodeposition. *Appl. Surf. Sci.* **2018**, *440*, 1073–1082. [CrossRef]
13. Golden, T.D.; Shang, Y.; Wang, Q.; Zhou, T. Electrochemical Synthesis of Rare Earth Ceramic Oxide Coatings. *Adv. Ceram. Process.* **2015**, *4*, 1–26.
14. Hamlaoui, Y.; Pedraza, F.; Remazeilles, C.; Cohendoz, S.; Rébéré, C.; Tifouti, L.; Creus, J. Cathodic Electrodeposition of Cerium-Based Oxides on Carbon Steel from Concentrated Cerium Nitrate Solutions. Part, I. Electrochemical and Analytical Characterisation. *Mater. Chem. Phys.* **2009**, *113*, 650–657. [CrossRef]
15. Bouchaud, B.; Balmain, J.; Bonnet, G.; Pedraza, F. PH-Distribution of Cerium Species in Aqueous Systems. *J. Rare Earths* **2012**, *30*, 559–562. [CrossRef]
16. Li, Z.; Jia, D.; Zhang, W.; Li, Y.; Wang, M.; Zhang, D. Enhanced Photocatalytic Performance by Regulating the Ce^{3+}/Ce^{4+} Ratio in Cerium Dioxide. *Front. Chem. Sci. Eng.* **2024**, *18*, 31–44. [CrossRef]
17. Zhang, G.; Zhou, Y.; Yang, Y.; Kong, T.; Song, Y.; Zhang, S.; Zheng, H. Elucidating the Role of Surface Ce^{4+} and Oxygen Vacancies of CeO_2 in the Direct Synthesis of Dimethyl Carbonate from CO_2 and Methanol. *Molecules* **2023**, *28*, 3785. [CrossRef]
18. Sbera, T.; Nayak, H.; Rama Rao Medicherla, V.; Kumar Kamilla, S. Effect of Heat Treatment on Structural Properties of CeO_2 Prepared by Chemical-Route Method. *Mater. Today Proc.* **2023**, *74*, 1063–1067. [CrossRef]

19. Acosta-Silva, Y.J.; Castañedo-Perez, R.; Torres-Delgado, G.; Méndez-López, A.; Zelaya-Ángel, O. Effect of Annealing Temperature on Structural, Morphological and Optical Properties of CeO_2 Thin Films Obtained from a Simple Precursor Solution. *J. Solgel Sci. Technol.* **2017**, *82*, 20–27. [CrossRef]
20. Phokha, S.; Limwichean, S.; Horprathum, M.; Patthanasettakul, V.; Chananonnawathorn, C.; Eiamchai, P.; Chanlek, N.; Maensiri, S. Effect of Annealing Temperature on the Structural and Magnetic Properties of CeO_2 Thin Films. *Thin Solid Film.* **2020**, *704*, 138001–138009. [CrossRef]
21. Channei, D.; Phanichphant, S.; Nakaruk, A.; Mofarah, S.S.; Koshy, P.; Sorrell, C.C. Aqueous and Surface Chemistries of Photocatalytic Fe-Doped CeO_2 Nanoparticles. *Catalysts* **2017**, *7*, 45. [CrossRef]
22. Luo, Y.; Li, J.; Zhu, J.; Zhao, Y.; Gao, X. Fabrication of Condensate Microdrop Self-Propelling Porous Films of Cerium Oxide Nanoparticles on Copper Surfaces. *Angew. Chem. Int. Ed.* **2015**, *54*, 4876–4879. [CrossRef] [PubMed]
23. Prieur, D.; Bonani, W.; Popa, K.; Walter, O.; Kriegsman, K.W.; Engelhard, M.H.; Guo, X.; Eloirdi, R.; Gouder, T.; Beck, A.; et al. Size Dependence of Lattice Parameter and Electronic Structure in CeO_2 Nanoparticles. *Inorg. Chem.* **2020**, *59*, 5760–5767. [CrossRef] [PubMed]
24. Li, P.; Zhang, M.; Li, X.; Wang, C.; Wang, R.; Wang, B.; Yan, H. MOF-Derived NiO/CeO_2 Heterojunction: A Photocatalyst for Degrading Pollutants and Hydrogen Evolution. *J. Mater. Sci.* **2020**, *55*, 15930–15944. [CrossRef]
25. Ederer, J.; Janoš, P.; Šťastný, M.; Henych, J.; Ederer, K.; Slušná, M.Š.; Tolasz, J. Nanocrystalline Cerium Oxide for Catalytic Degradation of Paraoxon Methyl: Influence of CeO_2 Surface Properties. *J. Environ. Chem. Eng.* **2021**, *9*, 106229–106242. [CrossRef]
26. Liu, J.; Dou, Z.; Zhang, T. Preparation of Oxygen Vacancy-Controllable CeO_2 by Electrotransformation of a $CeCl_3$ Solution and Its Oxidation Mechanism. *Ceram. Int.* **2020**, *46*, 5976–5982. [CrossRef]
27. Silva, I.D.C.; Sigoli, F.A.; Mazali, I.O. Reversible Oxygen Vacancy Generation on Pure CeO_2 Nanorods Evaluated by in Situ Raman Spectroscopy. *J. Phys. Chem. C* **2017**, *121*, 12928–12935. [CrossRef]
28. Zimou, J.; Nouneh, K.; Hsissou, R.; El-Habib, A.; Gana, L.E.l.; Talbi, A.; Beraich, M.; Lotfi, N.; Addou, M. Structural, Morphological, Optical, and Electrochemical Properties of Co-Doped CeO_2 Thin Films. *Mater. Sci. Semicond. Process.* **2021**, *135*, 106049–106061. [CrossRef]
29. Li, L.; Chen, F.; Lu, J.-Q.; Luo, M.-F. Study of Defect Sites in $Ce_{1-x}M_xO_{2-\delta}$ Solid Solutions Using Raman Spectroscopy. *J. Phys. Chem. A* **2011**, *115*, 7972–7977. [CrossRef]
30. Schilling, C.; Hofmann, A.; Hess, C.; Ganduglia-Pirovano, M.V. Raman Spectra of Polycrystalline CeO_2: A Density Functional Theory Study. *J. Phys. Chem. C* **2017**, *121*, 20834–20849. [CrossRef]
31. Bonu, V.; Das, A.; Sardar, M.; Dhara, S.; Tyagi, A.K. Surface Functionalization-Enhanced Magnetism in SnO_2 Nanoparticles and Its Correlation to Photoluminescence Properties. *J. Mater. Chem. C Mater.* **2015**, *3*, 1261–1267. [CrossRef]
32. Bortamuly, R.; Konwar, G.; Boruah, P.K.; Das, M.R.; Mahanta, D.; Saikia, P. CeO_2-PANI-HCl and CeO_2-PANI-PTSA Composites: Synthesis, Characterization, and Utilization as Supercapacitor Electrode Materials. *Ionics* **2020**, *26*, 5747–5756. [CrossRef]
33. Ankita, A.; Chahal, S.; Singh, S.; Kumar, S.; Kumar, P. Europium-Doped Cerium Oxide Nanoparticles: Investigating Oxygen Vacancies and Their Role in Enhanced Photocatalytic and Magnetic Properties. *Environ. Sci. Pollut. Res. Int.* **2024**, *31*, 1276–1287. [CrossRef] [PubMed]
34. Idriss, H. On the Wrong Assignment of the XPS O1s Signal at 531–532 EV Attributed to Oxygen Vacancies in Photo- and Electro-Catalysts for Water Splitting and Other Materials Applications. *Surf. Sci.* **2021**, *712*, 121894–121900. [CrossRef]
35. Morgan, D.J. Photoelectron Spectroscopy of Ceria: Reduction, Quantification and the Myth of the Vacancy Peak in XPS Analysis. *Surf. Interface Anal.* **2023**, *55*, 845–850. [CrossRef]
36. Ahmadizadeh, N.; Najafisayar, P. The Effects of Electrodeposition Parameters on the Wetting Behavior of Ceria Coatings. *Ceram. Int.* **2020**, *46*, 19583–19592. [CrossRef]
37. Qian, L.; Xu, F.; Voisey, K.T.; Nekouie, V.; Zhou, Z.; Silberschmidt, V.V.; Hou, X. Incorporation and Evolution of ZrO_2 Nano-Particles in Pt-Modified Aluminide Coating for High Temperature Applications. *Surf. Coat. Technol.* **2017**, *311*, 238–247. [CrossRef]
38. Mao, J.; Duan, X.; Yao, A. Influence of Sodium Dodecyl Sulfate on the Microstructure and Electrochromic Performance of an Electrodeposited Nickel Oxide Film. *Aust. J. Chem.* **2019**, *72*, 957–963. [CrossRef]
39. André, R.F.; Rousse, G.; Sassoye, C.; Avdeev, M.; Lassalle-Kaiser, B.; Baptiste, B.; Carenco, S. From $Ce(OH)_3$ to Nanoscaled CeO_2: Identification and Crystal Structure of a Cerium Oxyhydroxide Intermediate Phase. *Chem. Mater.* **2023**, *35*, 5040–5048. [CrossRef]
40. Choudhury, B.; Chetri, P.; Choudhury, A. Annealing Temperature and Oxygen-Vacancy-Dependent Variation of Lattice Strain, Band Gap and Luminescence Properties of CeO_2 Nanoparticles. *J. Exp. Nanosci.* **2015**, *10*, 103–114. [CrossRef]
41. Shirzad Choubari, M.; Mazloom, J.; Ghodsi, F.E. Supercapacitive Properties, Optical Band Gap, and Photoluminescence of CeO_2–ZnO Nanocomposites Prepared by Eco-Friendly Green and Citrate Sol-Gel Methods: A Comparative Study. *Ceram. Int.* **2022**, *48*, 21385–21395. [CrossRef]
42. Pelli Cresi, J.S.; Di Mario, L.; Catone, D.; Martelli, F.; Paladini, A.; Turchini, S.; D'Addato, S.; Luches, P.; O'Keeffe, P. Ultrafast Formation of Small Polarons and the Optical Gap in CeO_2. *J. Phys. Chem. Lett.* **2020**, *11*, 5686–5691. [CrossRef] [PubMed]
43. Isik, M.; Delice, S.; Gasanly, N.M. Temperature Dependence of Band Gap of CeO_2 Nanoparticle Photocatalysts. *Phys. E Low Dimens. Syst. Nanostruct.* **2023**, *150*, 115712–115717. [CrossRef]
44. Tang, J.; Han, Z.; Zuo, Y.; Tang, Y. A Corrosion Resistant Cerium Oxide Based Coating on Aluminum Alloy 2024 Prepared by Brush Plating. *Appl. Surf. Sci.* **2011**, *257*, 2806–2812. [CrossRef]

45. Ma, R.; Zhang, S.; Li, L.; Gu, P.; Wen, T.; Khan, A.; Li, S.; Li, B.; Wang, S.; Wang, X. Enhanced Visible-Light-Induced Photoactivity of Type-II CeO_2/g-C_3N_4 Nanosheet toward Organic Pollutants Degradation. *ACS Sustain. Chem. Eng.* **2019**, *7*, 9699–9708. [CrossRef]
46. Rani, N.; Ahlawat, R.; Goswami, B. Annealing Effect on Bandgap Energy and Photocatalytic Properties of CeO_2–SiO_2 Nanocomposite Prepared by Sol-Gel Technique. *Mater. Chem. Phys.* **2020**, *241*, 122401–122411. [CrossRef]
47. Shabalina, A.V.; Gotovtseva, E.Y.; Belik, Y.A.; Kuzmin, S.M.; Kharlamova, T.S.; Kulinich, S.A.; Svetlichnyi, V.A.; Vodyankina, O.V. Electrochemical Study of Semiconductor Properties for Bismuth Silicate-Based Photocatalysts Obtained via Hydro-/Solvothermal Approach. *Materials* **2022**, *15*, 4099. [CrossRef]
48. Du, J.; Chen, W.; Wu, G.; Song, Y.; Dong, X.; Li, G.; Fang, J.; Wei, W.; Sun, Y. Evoked Methane Photocatalytic Conversion to C2 Oxygenates over Ceria with Oxygen Vacancy. *Catalysts* **2020**, *10*, 196. [CrossRef]
49. Jiang, H.; Li, X.; Chen, S.; Wang, H.; Huo, P. G-C3N4 Quantum Dots-Modified Mesoporous CeO_2 Composite Photocatalyst for Enhanced CO_2 Photoreduction. *J. Mater. Sci. Mater. Electron.* **2020**, *31*, 20495–20512. [CrossRef]
50. Zheng, X.; Chen, Q.; Lv, S.; Fu, X.; Wen, J.; Liu, X. Enhanced Visible-Light Photocatalytic Activity of Ag QDs Anchored on CeO_2 Nanosheets with a Carbon Coating. *Nanomaterials* **2019**, *9*, 1643. [CrossRef]
51. Tian, N.; Huang, H.; Liu, C.; Dong, F.; Zhang, T.; Du, X.; Yu, S.; Zhang, Y. In Situ Co-Pyrolysis Fabrication of CeO_2/g-C_3N_4 n–n Type Heterojunction for Synchronously Promoting Photo-Induced Oxidation and Reduction Properties. *J. Mater. Chem. A* **2015**, *3*, 17120–17129. [CrossRef]
52. Lu, X.; Zheng, D.; Zhang, P.; Liang, C.; Liu, P.; Tong, Y. Facile Synthesis of Free-Standing CeO_2 Nanorods for Photoelectrochemical Applications. *Chem. Commun.* **2010**, *46*, 7721–7723. [CrossRef]
53. Sridharan, M.; Kamaraj, P.; Vennila, R.; Huh, Y.S.; Arthanareeswari, M. Bio-Inspired Construction of Melanin-like Polydopamine-Coated CeO_2 as a High-Performance Visible-Light-Driven Photocatalyst for Hydrogen Production. *New J. Chem.* **2020**, *44*, 15223–15234. [CrossRef]
54. Mehdi, M.; Karimi, H.; Ghaedi, M. CeO_2 Nanofibers-CdS Nanostructures n–n Junction with Enhanced Visible-Light Photocatalytic Activity. *Arab. J. Chem.* **2020**, *13*, 7583–7597. [CrossRef]
55. Sivula, K.; Sekar, A.; Moreno-Naranjo, J.M.; Liu, Y.; Yum, J.H.; Darwich, B.P.; Cho, H.H.; Guijarro, N.; Yao, L. Bulk Heterojunction Organic Semiconductor Photoanodes: Tuning Energy Levels to Optimize Electron Injection. *ACS Appl. Mater. Interf.* **2022**, *14*, 8191–8198.
56. Bredar, A.R.C.; Chown, A.L.; Burton, A.R.; Farnum, B.H. Electrochemical Impedance Spectroscopy of Metal Oxide Electrodes for Energy Applications. *ACS Appl. Energy Mater.* **2020**, *3*, 66–98. [CrossRef]
57. Anantha, M.S.; Dinesh, A.; Kundu, M.; Rani, M.; Venkatesh, K.; Raghu, M.S.; Yogesh Kumar, K.; Muralidhara, H.B. Single Step Assemble of Cerium Oxide Embellished on Layered Graphene Oxide: An Efficacious Electrode for Supercapacitors and Hydrogen Evolution Reaction. *Mater. Sci. Eng. B* **2022**, *284*, 115924–115935. [CrossRef]
58. Makarava, I.; Esmaeili, M.; Kharytonau, D.S.; Pelcastre, L.; Ryl, J.; Bilesan, M.R.; Vuorinen, E.; Repo, E. Influence of CeO_2 and TiO_2 Particles on Physicochemical Properties of Composite Nickel Coatings Electrodeposited at Ambient Temperature. *Materials* **2022**, *15*, 5550. [CrossRef]
59. Brug, G.J.; GVan Den Eeden, A.L.; Sluyters-rehbach, M.; Sluyters, J.H. The analysis of electrode impedances complicated by the presence of a constant phase element. *J. Electroanal. Chem.* **1984**, *176*, 275–295. [CrossRef]
60. Zamiri, R.; Ahangar, H.A.; Kaushal, A.; Zakaria, A.; Zamiri, G.; Tobaldi, D.; Ferreira, J.M.F. Dielectrical Properties of CeO_2 Nanoparticles at Different Temperatures. *PLoS ONE* **2015**, *10*, e0122989.
61. Lu, Y.; Mi, Y.; Li, J.; Qi, F.; Yan, S.; Dong, W. Recent Progress in Semiconductor-Ionic Conductor Nanomaterial as a Membrane for Low-Temperature Solid Oxide Fuel Cells. *Nanomaterials* **2021**, *11*, 2290. [CrossRef] [PubMed]
62. Korjenic, A.; Raja, K.S. Electrochemical Stability of Fluorine Doped Tin Oxide (FTO) Coating at Different PH Conditions. *J. Electrochem. Soc.* **2019**, *166*, 169–184. [CrossRef]
63. Đorđević, M.P.; Vukoje, I.; Lazić, V.; Đorđević, V.; Sredojević, D.; Dostanić, J.; Lončarević, D.; Ahrenkiel, S.P.; Belić, M.R.; Nedeljković, J.M. Electronic Structure of Surface Complexes between CeO_2 and Benzene Derivatives: A Comparative Experimental and DFT Study. *Mater. Chem. Phys.* **2019**, *236*, 121816–121824. [CrossRef]
64. Shi, L.; Zhuo, S.; Abulikemu, M.; Mettela, G.; Palaniselvam, T.; Rasul, S.; Tang, B.; Yan, B.; Saleh, N.B.; Wang, P. Annealing Temperature Effects on Photoelectrochemical Performance of Bismuth Vanadate Thin Film Photoelectrodes. *RSC Adv.* **2018**, *8*, 29179–29188. [CrossRef] [PubMed]

Disclaimer/Publisher's Note: The statements, opinions and data contained in all publications are solely those of the individual author(s) and contributor(s) and not of MDPI and/or the editor(s). MDPI and/or the editor(s) disclaim responsibility for any injury to people or property resulting from any ideas, methods, instructions or products referred to in the content.